Proximal lava drainage controls on basaltic fissure eruption dynamics

T.J. Jones[1*], E.W. Llewellin[1], B.F. Houghton[2], R.J. Brown[1] and C. Vye-Brown[3]

[1] Department of Earth Sciences, Durham University, South Road, Durham, DH1 3LE, UK
[2] Department of Geology & Geophysics, SOEST, University of Hawai'i at Mānoa, Honolulu, HI 96822, USA
[3] British Geological Survey, The Lyell Centre, Research Avenue South, Edinburgh, EH14 4AP, UK

***Corresponding author**: t.j.jones@durham.ac.uk

Key words: Mauna Ulu; vent localisation; lava ponding; lava tree moulds; eruption longevity; vent inundation.

Revised submission to Bulletin of Volcanology: 12th September 2017

Abstract

Hawaiian basaltic eruptions commonly initiate as a fissure, producing fountains, spattering, and clastogenic lava flows. Most fissures rapidly localize to form a small number of eruptive vents, the location of which may influence the subsequent distribution of lava flows and associated hazards. We present results from a detailed field investigation of the proximal deposits of episode 1 of the 1969 fissure eruption of Mauna Ulu, Kīlauea, Hawai'i. Exceptional preservation of the deposits allows us to reconstruct vent-proximal lava drainage patterns, and to assess the role that drainage played in constraining vent localization. Through detailed field mapping, including measurements of the height and internal depth of lava tree moulds, we reconstruct high-resolution topographic maps of the pre-eruption ground surface, the lava high-stand surface, and the post-eruption ground surface. We calculate the difference in elevation between pairs of maps to estimate the lava inundation depth and lava drainage depth over the field area, and along different segments of fissure. Aerial photographs collected during episode 1 of the eruption allows us to locate those parts of the fissure that are no longer exposed at the surface. By comparing with the inundation and drainage maps, we find that fissure segments that were inundated with lava to greater depths (typically 1-6 m) during the eruption later became foci of lava drainage back into the fissure (internal drain-back). We infer that, in these areas, lava ponding over the fissure suppressed discharge of magma, thereby favouring drain-back and stagnation. By contrast, segments with relatively shallow inundation (typically less than ~1 m), such as where the fissure intersects pre-eruptive topographic highs, or where flow away from the vent (outflow) was efficient, are often associated with sub-circular vent geometries in the post-eruption ground surface. We infer that these parts of the fissure became localization points for on-going magma ascent and discharge. We conclude that lava inundation and

56 drainage processes in basaltic fissure eruptions can play an important role in controlling
57 their localization and longevity.

Introduction

Basaltic fissure eruptions account for the bulk of the Earth's magma output (Sigurdsson 2000). Although relatively common, their deposits can nonetheless be challenging to investigate and interpret. Vent structures are known to evolve and migrate during eruptions (e.g. Richter et al. 1970; Thorarinsson et al. 1973; Swanson et al. 1979; Bruce and Huppert 1989), however evidence of these dynamic processes is commonly buried beneath later syn-eruptive material, including spatter, tephra fall, and subsequent lava flows (e.g. Thordarson and Self 1993; Larsen 2000; Brown et al. 2015; Reynolds et al. 2016). Furthermore, evidence of clastogenic eruption processes, such as spattering and fountaining, can be lost if pyroclastic material becomes agglutinated and/or forms rheomorphic lava flows (Sumner et al. 2005; Valentine and Gregg 2008; Parcheta et al. 2012).

Basaltic fissure eruptions typically initiate as curtains of fountaining basaltic spatter, bombs, and lapilli, with heights of 10's to 100's of meters (e.g. Richter et al. 1970; Swanson et al. 1979; Wolfe et al. 1988; Alparone et al. 2003). The vents are initially of high aspect ratio, with crack widths varying from ~ 2 m to tens of meters, and lengths ranging from several hundred metres to several kilometres (e.g. Gudmundsson 1987; Opheim and Gudmundsson 1989; Keating et al. 2008; Parcheta et al. 2015). Over the order of hours, the curtain generally focuses to a few point sources along the fissure (e.g. Richter et al. 1970; Thorarinsson et al. 1973; Swanson et al. 1979), however controls on the temporal and spatial evolution of such systems are poorly understood (Bruce and Huppert 1989). Progressive localisation causes a change in the eruption parameters, such as an increase in fountain height (Wilson et al. 1995), restricted spatial distributions of lava discharge

(Pedersen et al. 2017), and release of hazardous gases and aerosols (Walker et al. 1984; Stothers et al. 1986; Woods 1993) from a point, rather than a line, source. To track, and thus effectively manage, this dynamic situation, a better understanding of factors modulating fissure localisation is required.

Previous studies of vent localisation and termination of basaltic fissure eruptions have focused on thermo-rheological effects and the solidification of magma in the feeder dyke. Delaney and Pollard (1982) calculated that magma flowing at 1 ms^{-1} in a 2 m wide dyke should rapidly cool and solidify inwards from conduit margins to close the dyke within a few hours. They inferred that, for eruptions to last longer than a few hours, as observed in Iceland (Thorarinsson et al. 1973) and Hawai'i (Swanson et al. 1979), the width of the ascending dyke must be greater than 2 m. Bruce and Huppert (1989) investigated the role of thermo-rheological effects in vent-localization. They showed that the balance between heat transfer by advection and conduction governs whether conduit walls are melted back, widening the conduit, or magma solidifies against the walls, narrowing and eventually blocking the conduit (Bruce and Huppert 1989; Bruce and Huppert 1990). More recent work has shown that, as the magma cools against the wall rock, local regions of relatively cooler, higher viscosity magma are formed (Wylie and Lister 1995; Wylie et al. 1999). The fresh, hotter upwelling magma will tend to minimize energy loss by flowing through the regions of lowest viscosity, forming fingers of localized upwelling (Whitehead and Helfrich 1991; Helfrich 1995; Wylie and Lister 1995; Wylie et al. 1999).

Flow organization within basaltic feeder systems must also be influenced by drain-back of dense, degassed magma into the conduit. Drain-back has been documented at several lava

lakes, such as at Halema‘uma‘u Crater, Kīlauea Iki, and Makaopuhi on Kīlauea, Hawai’i (Wright et al. 1968; Richter et al. 1970; Swanson et al. 1979; Stovall et al. 2009; Patrick et al. 2015), Mt Erebus, Antarctica (e.g., Oppenheimer and Kyle 2008), and Erta Ale, Ethiopia (Oppenheimer and Francis 1997). At these systems fluctuations in the height of a lava lake have been related to pressure changes, magma flux or gas flux within the magma plumbing system (e.g., Tilling 1987; Witham and Llewellin 2006; Patrick et al. 2015). Bidirectional flow induced by the descent of relatively degassed, dense magma in a conduit has been investigated for the case of a vertical, cylindrical conduit geometry, and the upwelling and downwelling components organize either as core-annular flow, or side-by-side flow, depending on the viscosity ratio (Kazahaya et al. 1994; Stevenson and Blake 1998; Huppert and Hallworth 2007; Beckett et al. 2011; Palma et al. 2011; Beckett et al. 2014). Bidirectional flow has also been inferred from mass balance calculations at lava lakes; that is, to maintain a non-overflowing lake supply into the lake must be balanced by flow back down the conduit (Tilling 1987; Harris et al. 1999; Witham and Llewellin 2006; Harris 2008).

In some cases, lava has been directly observed to drain back down a fissure system, such as the 2002 eruption of Nyiragongo (Allard et al. 2002; Wunderman 2002); 1974 eruption of Kīlauea (Tilling et al. 1987; Wilson et al. 1995), and the 2011 Kamoamoa eruption (Orr et al. 2015). Drainage has also been inferred from studies of exposed vent deposits and dyke feeder systems at a range of depths (Lefebvre et al. 2012; Geshi and Neri 2014; Wadsworth et al. 2015). At greater depths, regions of both upwards and downwards flow have been identified within a single camptonite dyke at Higby Mountain, Connecticut (Philpotts and Philpotts 2007).

The role that drain-back plays in the evolution of magma flow organization within, and out of, a dyke is currently an open research question. Here, we use field evidence to investigate the inundation and drainage of basaltic lava during episode 1 of the 1969-74 eruption of Mauna Ulu, Hawai'i, USA, and assess its influence on shallow conduit dynamics and the spatio-temporal evolution of the fissure system.

Background

The Mauna Ulu 1969-74 eruption

Mauna Ulu is a small lava shield, located on the East Rift Zone (ERZ) of Kīlauea volcano, Hawai'i (Fig. 1a). The 1969–74 Mauna Ulu eruption that built this shield was characterized by two phases: Phase I began on May 24th 1969 and ended on October 15th 1971 during which 185 × 10^{6} m^{3} of lava were erupted (Swanson et al. 1979); and Phase II lasted from February 3rd 1972 to July 22nd 1974 (Tilling et al. 1987). The two phases were documented by Swanson et al. (1979) and Tilling et al. (1987) respectively. Here we follow the narrative of Swanson et al. (1979) and enhanced timings of (Parcheta et al. 2012). Episode 1 of the eruption initiated on May 24th 1969 with an earthquake swarm that could be felt in the nearby village of Volcano. At 04:45 Hawaiian Standard Time (HST) fountaining began from a newly formed fissure system close to 'Ālo'i Crater. This fissure rapidly propagated westwards, crossing the old Chain of Craters Road by 05:00 HST, and 'Āinahou Road (the current Chain of Craters Road; Fig. 1) at 08:30 HST, beyond which it exploited the Koa'e fault system, and terminated ~ 150m west of 'Āinahou Road. Steady fountaining and lava ponding occurred until 12:00 – 13:00 HST. During this time a pāhoehoe lava field advanced southward down slope from the fissure and ponded 1.2 km from the vent at the base of the north-facing Kalanaokuaiki Pali fault scarp (Fig. 1). Steady fountaining was followed by a

period of waning activity and lava drain-back ending at 22:00 HST. This marked the end of episode 1, and the last eruptive activity in the western segment of the Mauna Ulu fissure system. All subsequent activity occurred further to the east, forming the Mauna Ulu shield and its associated lava flow field. Most significantly for this study, a voluminous lava flow in January-March 1974, originating from the Mauna Ulu shield, covered large sections of the originally 4.5 km long fissure, leaving only the 880 m long western section exposed and available to study today (Figs. 1b, c). Therefore, this study solely focuses on the early development of the fissure system rather than the later phases that were confined to the Mauna Ulu shield to the east; all discussions of lava re-surfacing refer to the 1969 episode 1 eruption. Contemporary observation of episode 1 was limited to eye-witness accounts by HVO scientists (Swanson et al. 1979) and aerial photographs taken serendipitously by a Sandia Labs aerial survey (now held at the USGS Hawaiian Volcano Observatory; Figure S1) taken one hour after the fissure system reached its full length (Swanson et al. 1979; Parcheta et al. 2012).

Previous mapping of the episode 1 fissure system

The exceptional preservation of the episode 1 fissure system offers a unique opportunity to investigate shallow conduit geometries and processes. Parcheta et al. (2015) used ground-based LiDAR to measure the geometry of parts of the shallow conduit (< 15 m depth) and vents associated with the episode 1 fissure system. They mapped 54 vents or fissure segments along the surviving 880 m of fissure and document several distinct geometric features including: (1) five en echelon steps caused by the rotation of a rectilinear dyke to a near-shear stress orientation upon ascent; (2) sinuous individual fissure segments most likely related to stress field interactions between the ERZ and the Koa‘e fault system, as well

as fissure irregularity; and (3) irregularity in the internal dyke wall surface, thought to represent pre-existing cooling joints within the pre-1969 lava flow through which the dyke cuts (Parcheta et al. 2015). Three-dimensional imaging of the subsurface vent structures showed that the primary conduit wall consists of jigsaw-like fits between either side of the conduit (Parcheta et al. 2016), indicating that the conduit walls have not been modified since the eruption.

The vent geometries range from sub-circular to linear in plan-view, and from parallel-sided to flared in cross-section. The degree of vent flaring was characterised quantitatively through the LiDAR point cloud for three vents (Parcheta et al. 2015). No clear relationship between fountain height and vent flaring was found, although fountain height during the eruption was poorly quantified. Parcheta et al. (2015) suggested that the flaring was caused by either syn-eruptive erosion or late-stage drain-back of ponded lava.

Methods

Fieldwork

In this study we focus on the near-fissure products of the episode 1 flow field (Fig. 1c). At the time of the eruption this area was densely forested, and the episode 1 lava flows quenched against the trees. As the flows inflated, the quench surface extended higher up the trees, forming casts up to 5 m high; this lava high-stand surface represents the maximum local inundation depth (Parcheta et al., 2015). During the waning stage of the eruption, lava drained to leave solidified lava quenched against the tree to form a tree mould (Finch 1931; Moore and Richter 1962; Lockwood and Williams 1978; Lockwood and Lipman 1980). The difference in height between the lava high-stand surface and final, post-

eruption ground surface represents the extent of drainage from the maximum inundation depth, termed the lava drainage depth (Finch 1931; Moore and Richter 1962; Lockwood and Williams 1978; Parcheta et al. 2015). The entire area was densely forested, hence tree moulds provide a consistent dataset for inundation depth across the proximal lava flow field fed by the episode 1 fissure.

Measurements of elevation of the lava high-stand (syn-eruption) surface and post-eruption ground surface (i.e. the present day surface) were taken using a Leica SR520 kinematic GPS (kGPS) on > 200 tree moulds (Fig. 2). The following measurements were made for each tree mould, where possible: (1) internal depth of the tree mould (by lowering a plumb-bob into the mould); (2) elevation of the uppermost crust level (lava high-stand); (3) elevation of the post-eruption ground surface around the tree mould (i.e. the level of the surface following drainage); (4) height of the top of the tree mould above the surrounding lava surface. Note this final measurement is the same as the difference between measurements 2 and 3, and is therefore redundant in some locations. Measurements are summarized in Figure 2. We note that a tree mould's internal depth is subject to error if debris has fallen down the cast, therefore measurements are only reported where a soil horizon was hit by the plumb bob. In the field, the soil horizon was identified either by visual inspection if the tree mould was shallow, from the sound heard upon contact, or from the presence of soil on the plumb bob. Estimated accuracy of the tree mould depth measurement is ± 2 cm. The location of a specific point within the field area was re-measured seven times using our standard kGPS protocol, enabling quantification of uncertainty in the measured position associated with data acquisition and processing. We obtained a standard deviation of 0.012 m, 0.017 m and 0.018 m, for the E–W, N–S and vertical positions, respectively.

224

225 *Map production*

226 A geo-referenced database relating all attributes (tree mould height and depth) to their
227 associated kGPS location was created. These data were then imported into a geographic
228 information systems program (ArcGIS™) for all further analysis. Interpolation to produce a
229 raster map was performed using the tension spline interpolation routine. This routine bends
230 a surface through the known input data points whilst trying to minimize the total curvature
231 of the surface. In a *tension* spline both first and second derivatives terms are used to
232 minimize the curvature of the surface (Franke 1982; Mitáš and Mitášová 1988). We used the
233 routine with 10 points per region and $\phi = 1$, where ϕ is the weight given to the first
234 derivative term and can be thought of as the "surface stiffness" (Franke 1982). This
235 approach was used to create topographic maps for: (1) the pre-eruption ground surface; (2)
236 the lava high-stand surface; and (3) the post-eruption ground surface. These maps were
237 produced from the following data (Fig. 2): (1) the kGPS positions of the uppermost crust
238 minus the measured tree mould depth, (2) the kGPS positions of the uppermost crust and
239 (3) the kGPS positions of the post-eruption ground surface respectively.

240 The three topographic surface maps were used to create two further maps: (1) a map of
241 lava inundation depth during eruption, and (2) a map of lava drainage depth. The map of
242 lava inundation was created by subtracting the pre-eruption ground surface raster map
243 from the lava high-stand surface raster map using the ArcMap™ 3D Analyst minus tool. The
244 map of lava drainage depth was created by subtracting the post-eruption ground surface
245 raster map from the lava high-stand surface raster map. We note that it is possible that lava
246 may have compacted slightly post-emplacement. Because our data do not allow us to

247 quantify this process, it must be considered as a potential source of additional uncertainty
248 on lava drainage. Note that, for completeness, we also produce a map of residual lava
249 thickness, presented as Figure S2 in the supplementary information, by subtracting the pre-
250 eruption ground surface raster map from the post-eruption surface raster map. The
251 distribution of residual lava thickness is not discussed further in this work.

252 *Profile production*

253 One of the goals of our study is to investigate how measured parameters, such as
254 inundation depth, vary along the fissure. This is complicated by the fact that the fissure is
255 discontinuous, and is divided into roughly parallel-trending segments that are offset from
256 one another perpendicular to strike. To create a continuous profile along the entire length
257 of the fissure system we project each segment of the fissure onto a single line with the same
258 overall trend as the fissure system, where the overall trend line is taken as the line
259 connecting the locations of the western-most and eastern-most fissure exposures. The
260 process is illustrated in Figure 3. As part of the process, we first geo-referenced the aerial
261 photograph taken by Sandia Labs (Figure S1) and marked the active fissure segments onto
262 the topographic maps. Next, to link all the discontinuous en echelon segments, we
263 determined the overall trend line for the system, which has bearing 079.365°. From the end
264 of each segment, a tie-line was drawn perpendicular to the overall trend line, then the
265 midpoint between the tie-lines, on the overall trend line, was located. Lastly, the segment
266 trend lines were extended within each gap until they met at the midpoint. Parameters were
267 then projected onto the overall trend line to create a continuous profile along strike,
268 allowing us to investigate trends that occur along the entire eruptive fissure.

269

Results

Topographic maps

Figure 4a shows a map of the pre-eruption ground surface topography prior to the 1969 Mauna Ulu eruption, reconstructed from tree mould depths. Overall the ground elevation slopes to the south, consistent with the regional trend on the southern flank of the Kīlauea shield. The broad trends in the map are also consistent with the relatively low resolution topographic map (1:24,000 scale; 6.1 m vertical resolution) produced by the United States Geological Survey (USGS) before the 1969 eruption (Plate 1 of Swanson et al. 1979). Note that our absolute elevation values differ from those of Swanson et al. (1979) because we use a different vertical reference datum: Swanson et al. (1979) use a vertical reference of mean sea level whereas we use the WGS 84 reference ellipsoid. In detail, the pre-eruption topography has two broad depressions in the east of the mapped area, starting close to the fissure and sloping southward. Close to the fissure these depressions are approximately 60 m wide and 1 m deep relative to surrounding topography. Away from the fissure, these depressions broaden to > 170 m and deepen to 4 m. There is a shallow elongate depression, approximately 70 m wide, in the northwest section of the field area. The depression strikes roughly NW–SE, and crosses the fissure (but note that there is no exposure of the fissure presently observable in this region). At a smaller scale, below the resolution of this measurement technique, we expect the pre-eruption ground surface to have had decimetre- and centimetre-scale variations caused by lava surface folding, changes in substrate (e.g., road vs. vegetation) and varying pre-existing lava type (e.g. shelly pāhoehoe vs. ropy pāhoehoe etc.).

The lava high-stand surface (Fig. 4b) also has an overall southward slope. By visual inspection of the contour spacing, this surface in general shows less topographic relief than the pre-eruption ground surface. The northwest region of the field area has the highest elevation (~998 m) and there is no clear evidence of the topographic depression observed in the north-west section of the pre-eruption map. The two eastern, south-trending depressions observed in the pre-eruption map can also be detected on this surface, though they are less prominent.

The post-eruption ground surface (i.e. the present day topography; Fig. 4c) is the most robust dataset because it has the highest density of kGPS points (black circles in Fig. 4c); it has been validated through visual comparison with a National Oceanic and Atmospheric Administration digital elevation model (2005 IfSAR DEM). The post-eruption ground surface also has an overall southward slope. In the west, a large, closed basin is present between exposed fissure segments, and in the central and eastern sections, several isolated depressions and topographic highs result in a more variable and steeper relief than that seen in Figures 4a and b.

Lava inundation

Figure 5 shows the lava inundation depth over the mapped area (i.e. the difference between the lava high-stand and pre-eruption ground surface). Much of the proximal lava flow field was inundated with a 1 to 3 m thickness of lava at peak height. Isolated regions of > 4 m thick lava are commonly associated with depressions in the pre-eruption topography (Fig. 4a).

Also shown on Figure 5 are segments of the fissure that are in eruption on the Sandia Labs aerial imagery. These segments appear as orange (incandescent) lines on the images. Segments were traced from the Sandia Labs aerial imagery and overlain onto our maps using Google Earth Pro™. Note that substantial parts of the fissure that were active in the images have no surface expression in the field today. Gaps in exposure of the fissure (Fig. 5) are generally associated with regions of relatively deep lava inundation. This is particularly evident in the western part of the fissure system, and at the prominent en echelon step just east of the centre of the fissure system (Fig. 5).

Drainage

Drainage depth varies between 0 and 4 m (Fig. 6). In the western part of the fissure system, drainage is greatest in the basin along fissure segments that once erupted (but are no longer exposed at the surface), removing a maximum of 3.0 m of lava at its centre. In the eastern part of the fissure system, several drainage regions are centred directly along fissure segments, and remove a maximum of ~ 3.5 m of lava. Some of these regions link southward into drainage channels (see Figs. 4a and c) and others form closed basins that are similar to, but smaller than, the western basin.

Interpretations

One of our goals is to understand and interpret the lava drainage patterns evidenced by the Mauna Ulu episode 1 field data. We define two terms to describe drainage: 'outflow' is the drainage of lava away from the fissure; 'drain-back' is the drainage of lava back into the fissure. To set the context for our interpretation of the results previously presented (Figs. 4–6) we introduce two hypothetical end-member scenarios. (1) If a region were completely

confined, with no pathway for the lava to drain away, then the lava would simply form a pond, and the high-stand surface would be flat and horizontal, with only minor perturbations that correspond to surface ropes and folding. (2) If all lava could freely drain either down slope, away from the fissure (outflow), or back down the conduit (drain-back), then the lava high-stand surface would reflect only dynamic ponding. These two end-member scenarios, of either widespread ponding or widespread drainage, constitute hypotheses against which we can evaluate the field data.

The situation during episode 1 of the 1969 Mauna Ulu eruption was more complex than these simple end-member scenarios. Whilst the lava high-stand surface in the western part of the fissure system was fairly flat, the eastern part adopted a broad south-sloping trend with smaller scale topographic depressions and highs (Fig. 4b). Additionally, lava inundation depth was not consistent along the fissure (Fig. 5): certain fissure segments, and the adjacent proximal flow field, experienced a deeper inundation above the vent than others. This suggests that, during the eruption, the proximal flow field was characterized by a complex and spatially variable inundation, including elements of both static and dynamic ponding. We explore these complexities in detail by comparing two regions of the proximal flow field. The first region is in the west of the field area (Box 1 in Fig. 7a) and has a lava high stand surface that is relatively flat and horizontal. It contains an unexposed eruptive fissure (Fig. 7b), and forms part of an isolated, closed basin in the pre-eruption topography. The second region is in the east of the field area (Box 2 in Fig. 7a) and has a lava high stand surface that consistently slopes to the south. It includes a prominent south-orientated channel in the pre-eruption topography.

Case study 1: Isolated western basin

The first case study location includes four fissure segments (Fig. 7b), all of which erupted material, but which are now either completely covered, with no surface expression, or are only partially exposed. Drainage is at a local maximum on and near the fissure (Fig. 7c). The drainage regions are isolated and do not continue downslope away from the fissure; hence, drainage must have occurred as internal, drain-back into the fissure, along segments that are no longer exposed at the surface. The topographic profile taken from the drainage map along the fissure in box 1 (Fig. 7d) reveals a maximum of 3 m of drainage (i.e. a 3 m reduction in ground elevation) in the central portion of the fissure, declining in both directions along fissure. The inundation profile along the same portion of the fissure (Fig. 7d) shows that the entire segment had material ponded over the fissure whilst it was erupting. The lava inundation reached a maximum of 3.9 m in the central portion of the fissure, and plateaued at ~2.2 m to the east. This region of deep lava inundation corresponds to an elongate depression in the pre-eruption topography (Fig. 4a). The inundation depths along the profile are roughly inversely correlated with the palaeo-depression's topography, which has its axis, and therefore deepest inundation, centred ~ 0.12 km from the western end of the fissure.

We infer that, as the episode 1 lava flow field developed, it flooded the isolated western palaeo-depression leading to deep inundation above the erupting fissure. At present there is a local, isolated depression in this area, indicating that, during the waning stages of the eruption, lava drained back down the fissure (Figs. 7c and 7e). The amount of drainage varies across the western basin but reaches a maximum between 0.1 and 0.16 km from the western end of the fissure. We hypothesise this could be because: (1) this was the deepest

389 part of the palaeo-depression, where the greatest thickness was available to drain; and/or,
390 (2) the depth of the lava allowed it to retain more heat and maintain a lower viscosity than
391 that in the surrounding flow field, hence it could drain more easily, or for longer.
392
393 *Case study 2: External and internal drainage*
394 For the second case study, we examine an area in the east of the field area, where the
395 Sandia Labs aerial imagery shows lava flows moving south, following pre-existing
396 topographic channels, away from the fissure vent (Fig. 8a and Box 2 of Fig. 7a). The drainage
397 map indicates that the drainage depth peaks twice along the fissure (Fig. 8b). Unlike case
398 study 1, there is no correlation between the location of the drainage maxima and the
399 location of areas of deepest lava inundation (Fig. 8b); therefore we cannot invoke the same
400 drainage mechanisms. To investigate further, we construct two profiles that crosscut the
401 fissure: (1) where it is now covered by lava, and hidden (A-A'); and (2) where it remains
402 exposed at the surface (B-B'). The pre-eruption ground surface across these two profile lines
403 has a different slope (Fig. 8c): profile A-A' has a shallower proximal gradient than profile B-
404 B'. We infer that, during the eruption, lava was more effectively drained away from the
405 vent-proximal region at fissure location B-B' because of the greater slope. In this area, lava
406 drainage mainly occurred down-slope away from the fissure (outflow), rather than internally
407 back into the fissure (drain-back). By contrast, the shallower slope at A-A' inhibited external,
408 down-slope outflow, hence lava either became dynamically ponded above the vent (when
409 magma supply exceeded outflow) or drained back down fissure.
410
411 **Discussion**

412 Tree mould mapping provides spatial information on lava drainage that allows us to
413 reconstruct activity at and around missing (buried) fissure segments. The part of the fissure
414 discussed in case study 1 (Fig. 7e) shows no indication of an eruptive vent, and has been
415 completely covered by episode 1 lava. Our mapping approach, and the subsequent
416 production of a drainage map, provides a way to constrain the location of the eruptive
417 fissure in the absence of direct observations. It also suggests that calculations of eruptive
418 volume based on the present aerial extent and thickness of deposits are a minimum,
419 because they do not consider erupted material that has drained back down a vent during
420 waning stages.
421
422 The two case studies indicate that lava ponded over segments of the fissure either statically,
423 as a result of topographic confinement (case study 1), or dynamically, because magma
424 supply temporarily exceeded outflow (section cut by line A-A', case study 2). In both cases,
425 deep ponding is associated with no exposure of the fissure post-eruption. This suggests that
426 the extent of the lava cover over an erupting vent, in turn a function of pre-eruption
427 topography and the local eruption and outflow fluxes, may influence whether or not it will
428 be preserved post-eruption, with deeply flooded vents less likely to be preserved. To
429 understand the physical rationale for this interpretation, we must consider the effect that
430 ponding has on eruption through an inundated linear vent.
431
432 The eruption of spatter through ponded lava was observed directly during the March 2011
433 Kamoamoa fissure eruption at Kīlauea (Lundgren et al. 2013; Orr et al. 2015). In this case,
434 ponding "drowned" the fissure and locally suppressed eruptive activity (Orr et al. 2015).
435 Slow-moving magma in a fissure loses its heat to the country rock more effectively than fast-

436 flowing magma, hence its viscosity increases, leading to a positive feedback that promotes
437 stagnation and blocking of the most sluggish portions of a fissure (Bruce and Huppert 1989).
438 This supports a hypothesis that ponding acts to suppress the eruption in that location
439 indirectly by reducing mass flux and causing magma within the underlying section of fissure
440 to slow its ascent. We further contend that fissure eruptions are likely to be particularly
441 susceptible to flow perturbations induced by ponding, because ascending magma can flow
442 laterally to bypass regions of stagnant or down-welling magma more easily than is the case
443 for a circular conduit/vent geometry.
444
445 Wilson et al. (1995) present an analysis of the eruption of basaltic magma from a linear
446 fissure vent, through a lava pond, determining the height of lava fountaining as a function of
447 pond depth, exsolved water content, and mass eruption rate. They consider only the effect
448 of the additional energy required to eject entrained lava into the fountain, and do not
449 consider thermo-rheological effects, nor along-fissure migration of flow in response to
450 along-strike variations in pressure gradients. Nonetheless, an analysis of the episode 1
451 eruption, following their approach, is instructive. Figure 9 shows estimates of fountain
452 height expected for the eruption as a function of ponding depth, based on data in Table 3 of
453 Wilson et al. (1995). The episode 1 mass eruption rate is estimated from Swanson et al.
454 (1979), who report bulk volumetric eruption rates of 1.30×10^5 m^3h^{-1} for episode 1 based on
455 the aerial extent and thickness of the lava flows it produced. Using an average lava flow
456 interior bulk density (1750 kgm^{-3}) that we measure from field samples, this equates to an
457 average mass eruption rate of 6.31×10^4 kgs^{-1}. To normalize the mass eruption rate to a unit
458 length of fissure, we measured the length of incandescent fissure (assumed to be erupting)
459 in the Sandia Labs aerial imagery, which were taken approximately one hour after the

460 fissure system had reached its full length. We found that ~ 1250 m of the original 4.5 km
461 fissure was erupting, giving a mass eruption rate per unit length of 50.5 $kgs^{-1}m^{-1}$. This value
462 represents an estimate of the average eruption rate through the whole of episode 1, and
463 neglects temporal variations, for instance during the waxing and waning stages of the
464 eruption; consequently, it should be taken as a minimum estimate of the typical eruption
465 rate when the fissure was at full length. We therefore take 10^2 $kgs^{-1}m^{-1}$ as an order-of-
466 magnitude estimate for comparison with the model curves of Wilson et al. (1995). We
467 estimate the water loss to be ~ 0.4 wt. %, calculated as the difference between the assumed
468 water content of basaltic melt at Kīlauea's shallow (1–3 km) summit reservoir (0.5 wt.%;
469 Moore 1970) and the water content of spatter from low fountains at Mauna Ulu (0.07 wt %;
470 Swanson and Fabbi 1973).

471

472 The results show that an increase in lava pond depth over a fissure strongly influences
473 fountain height (Fig. 9). A ponding depth of 0.5 m above the vent reduces the fountain
474 height by approximately two orders of magnitude compared with the pond-free case – from
475 around 150 m to around 5 m. At ponding depths ≥ 2 m, the fountaining height tends to zero.
476 We note, however, that at shallow ponding depths (≤ 0.3 m) the absolute heights of the lava
477 fountains calculated using the Wilson et al. (1995) approach are much greater than
478 indicated by contemporary field observations. Swanson et al. (1979) report observed
479 maximum fountain heights of 50 m, whilst Parcheta et al. (2012) inferred that fountain
480 heights ranged between 13 and 32 m, based on calibration of field photographs taken at the
481 time of the eruption. One interpretation of the discrepancy between the theoretical
482 calculations and the visual accounts is that all the vents were inundated to some degree.

Another possibility is that this discrepancy arises because the model calculations do not account for lateral migration of magma along strike. If flow were to focus laterally, the mass eruption rate would increase at the localization points, resulting in higher fountaining. An increase in ponding depth at one location might therefore lead to an increase in mass eruption rate (and increasing fountain height) in adjacent parts of the fissure.

Our contention that magma can migrate laterally in response to ponding is supported by analysis of episode 1 rampart material (Parcheta et al. 2012) and visual observations at the time of eruption (Swanson et al. 1979), which indicate that fountaining intensity varied laterally along strike and temporally throughout the eruption. For instance, at a single time, variations of 10 –15 m in fountain height were observed over short (4 – 15 m) distances along strike (Swanson et al. 1979; Parcheta et al. 2012). These variations are a result of the progressive vent localization process. To illustrate the effect that variable inundation can have on vent localization, we consider a third case study region within the central portion of the field area (Box 3; Fig. 7a). Here there are vents on two segments of fissure (X-Y and Y-Z) that initially erupted along their entire lateral extent (interpreted from Sandia Labs aerial imagery; Figure S1) but are today only preserved in limited sections (Fig. 10a). An extract from our lava inundation map (Fig. 10b) shows that the maximum thickness of lava above the vent is highly variable along strike. In this area the pre-eruption ground surface reaches a local minimum between the two fissure segments (Fig. 10c). The lava inundation profile across the region of interest (Fig. 10d) shows that ponding depth varies between 0.5 m and 3.5 m and reaches a maximum in the centre where the fissure is no longer exposed at the surface. This ponding depth range (0.5–3.5 m) is sufficient to result in a large reduction in

506 fountain height (Wilson et al. 1995). We suggest that deeper regions of lava ponding caused
507 by palaeo-topography at the east of fissure X-Y and the west of fissure Y-Z suppressed
508 fountaining in these regions, leading to blocking of the shallow conduit. This is consistent
509 with the observation that the vents are no longer visible, and are covered by 1969 lava. It is
510 also possible that proximity to the end of the fissure segments in this region contributed to
511 blocking of the conduit in this region.

512

513 Our observations and interpretations support the idea that ponding over the vent may
514 influence local eruption intensity and the longevity of an eruptive segment. In this model,
515 summarized in Figure 11, suppression of fountaining by deep ponding is followed by
516 stagnation of the eruption at that location, and/or drain-back of erupted lava into the
517 conduit. In either case, the viscosity of the magma in that part of the conduit increases,
518 resulting in early shut-down of the eruption at that fissure segment and decreasing the
519 likelihood of it being preserved as an open vent post-eruption. As a corollary, the location of
520 pre-eruption topographic highs intersected by the eruptive fissure appears to correspond
521 with preserved eruptive vents. These palaeo-topographic highs, along fissure from palaeo-
522 lows, have relatively shallow lava ponding depths, and are often associated with sub-circular
523 vent geometries. We infer that these parts of the fissure became focal points for ongoing
524 magma ascent and discharge, and that consequent mechanical erosion transformed the
525 fissure to a more circular geometry (Delaney and Pollard 1981; Wylie et al. 1999; Mitchell
526 2005).

527

528 We note that the topographic variation across the Mauna Ulu field site is fairly modest. The
529 pre-eruption ground surface elevation varies along the eruptive fissure by just a few metres
530 (Fig. 4). Furthermore, the mass eruption rates are low (~50 $kgs^{-1}m^{-1}$). Eruptions with more
531 extreme (~ 100 m) topographic variations and much higher mass eruption rates may
532 experience different controls on localisation to those discussed in this study.
533
534 **Conclusions**
535 Tree mould mapping allows the reconstruction of topographic maps for the ground/lava
536 surface before, during and after an eruption. These data can be combined to estimate: (1)
537 the depth of lava inundation above the eruptive vent and (2) the amount of drainage that
538 occurred since the lava high stand. This is particularly useful where syn-eruptive
539 observations are limited or non-existent. We use this technique to investigate the episode 1
540 fissure system of the 1969 Mauna Ulu eruption of Kīlauea, Hawai'i, and analyse its evolution
541 from laterally continuous Hawaiian fountaining, to more discrete vents, as fissure segments
542 narrowed and closed. Pre-eruption topography is an important control on the evolution of
543 this eruption (Fig. 11): we have shown that the suppression of fountaining by deep ponding
544 – either statically or dynamically – is followed by stagnation of the eruption at that location,
545 and/or drain-back of erupted lava into the conduit. In either case, the viscosity of the
546 underlying magma is expected to increase, resulting in early shut-down of the eruption at
547 that fissure segment and decreasing the likelihood of it being preserved as an open vent
548 post-eruption. In contrast, we have shown that parts of the fissure with shallow ponding,
549 such as palaeo-highs and regions where external drainage (outflow) is effective (Fig.11), are
550 the focal point of continued magma discharge and eruption. We therefore conclude that, in
551 addition to thermal-rheological controls, surface effects (lava inundation, pre-eruption

552 topography, and drainage) can play an important role in the evolution of a basaltic fissure
553 system. Finally, we propose that using the pre-eruption surface to predict the amount of
554 internal (drain-back) and external (outflow) drainage could be a useful tool in hazard
555 forecasting and assessment. For instance, knowing the relative proportion of drain-back and
556 outflow along a fissure could support prediction of the variation in eruption longevity at
557 specific locations along strike, allowing the vent localization pattern to be predicted.
558 Prediction of, or early identification of, those parts of a fissure along which outflow localizes
559 could, in turn inform source parameters for consequent lava flow hazard modelling.
560

561 **Acknowledgements**

562 Mike Poland is thanked for his support with the kGPS measurements and data processing.
563 Tim Orr and Carolyn Parcheta are thanked for their discussions from which this work
564 benefitted. TJJ is funded by NERC grant NE/L0025901, part of the IAPETUS doctoral training
565 partnership. EWL acknowledges support from NERC grant NE/N018443/1. CVB publishes
566 with the permission of the Executive Director of the British Geological Survey. We thank
567 Matt Patrick, Greg Valentine, the handling editor Jacopo Taddeucci and the executive editor
568 Andrew Harris for their comments that improved the manuscript.
569

570 **References:**

571 Allard P, Baxter P, Halbwachs M, Komorowski J-C (2002) The January 2002 eruption of
572 Nyiragongo volcano (Dem. Repub. Congo) and related hazards: observations and
573 recommendations. Final Report of the French-British Team, Paris (2002).
574 Alparone S, Andronico D, Lodato L, Sgroi T (2003) Relationship between tremor and volcanic
575 activity during the Southeast Crater eruption on Mount Etna in early 2000. J Geophys

576 Res Solid Earth. doi: 10.1029/2002JB001866
577 Beckett FM, Burton M, Mader HM, et al (2014) Conduit convection driving persistent
578 degassing at basaltic volcanoes. J Volcanol Geotherm Res 283:19–35.
579 Beckett FM, Mader HM, Phillips JC, et al (2011) An experimental study of low-Reynolds-
580 number exchange flow of two Newtonian fluids in a vertical pipe. J Fluid Mech
581 682:652–670.
582 Brown RJ, Thordarson T, Self S, Blake S (2015) Disruption of tephra fall deposits caused by
583 lava flows during basaltic eruptions. Bull Volcanol 77:90. doi: 10.1007/s00445-015-
584 0974-3
585 Bruce PM, Huppert HE (1989) Thermal control of basaltic fissure eruptions. Nature 342:665–
586 667.
587 Bruce PM, Huppert HE (1990) Solidification and melting along dykes by the laminar flow of
588 basaltic magma. In: Ryan MP (ed) Magma transport and storage. Wiley, pp 87–101
589 Delaney PT, Pollard DD (1982) Solidification of basaltic magma during flow in a dike. Am J Sci
590 282:856–885.
591 Delaney PT, Pollard DD (1981) Deformation of host rocks and flow of magma during growth
592 of minette dikes and breccia-bearing intrusions near Ship Rock, New Mexico. US Geol.
593 Surv. Prof. Paper 1202.
594 Finch RH (1931) Lava tree casts and tree molds. Volc Lett 316:1–3.
595 Franke R (1982) Smooth interpolation of scattered data by local thin plate splines. Comput
596 Math with Appl 8:273–281.
597 Geshi N, Neri M (2014) Dynamic feeder dyke systems in basaltic volcanoes: the exceptional
598 example of the 1809 Etna eruption (Italy). Front Earth Sci 2:13. doi:
599 10.3389/feart.2014.00013

600 Gudmundsson A (1987) Tectonics of the Thingvellir fissure swarm, SW Iceland. J Struct Geol
601 9:61–69. doi: http://dx.doi.org/10.1016/0191-8141(87)90044-7
602 Harris AJL (2008) Modeling lava lake heat loss, rheology, and convection. Geophys Res Lett.
603 doi: 10.1029/2008GL033190
604 Harris AJL, Flynn LP, Rothery DA, et al (1999) Mass flux measurements at active lava lakes:
605 implications for magma recycling. J Geophys Res Solid Earth 104:7117–7136.
606 Helfrich KR (1995) Thermo-viscous fingering of flow in a thin gap: a model of magma flow in
607 dikes and fissures. J Fluid Mech 305:219–238.
608 Huppert HE, Hallworth MA (2007) Bi-directional flows in constrained systems. J Fluid Mech
609 578:95–112.
610 Kazahaya K, Shinohara H, Saito G (1994) Excessive degassing of Izu-Oshima volcano: magma
611 convection in a conduit. Bull Volcanol 56:207–216.
612 Keating GN, Valentine GA, Krier DJ, Perry F V. (2008) Shallow plumbing systems for small-
613 volume basaltic volcanoes. Bull Volcanol 70:563–582. doi: 10.1007/s00445-007-0154-1
614 Larsen G (2000) Holocene eruptions within the Katla volcanic system, south Iceland:
615 characteristics and environmental impact. Jökull 49:1–28.
616 Lefebvre NS, White JDL, Kjarsgaard BA (2012) Spatter-dike reveals subterranean magma
617 diversions: Consequences for small multivent basaltic eruptions. Geology 40:423–426.
618 Lockwood JP, Lipman PW (1980) Recovery of datable charcoal beneath young lavas: lessons
619 from Hawaii. Bull Volcanol 43:609–615.
620 Lockwood JP, Williams IS (1978) Lava trees and tree moulds as indicators of lava flow
621 direction. Geol Mag 115:69–74.
622 Lundgren P, Poland M, Miklius A, et al (2013) Evolution of dike opening during the March
623 2011 Kamoamoa fissure eruption, Kīlauea Volcano, Hawai`i. J Geophys Res Solid Earth

118:897–914. doi: 10.1002/jgrb.50108

Mitáš L, Mitášová H (1988) General variational approach to the interpolation problem. Comput Math with Appl 16:983–992.

Mitchell KL (2005) Coupled conduit flow and shape in explosive volcanic eruptions. J Volcanol Geotherm Res 143:187–203.

Moore JG (1970) Water content of basalt erupted on the ocean floor. Contrib to Mineral Petrol 28:272–279.

Moore JG, Richter DH (1962) Lava tree molds of the September 1961 eruption, Kilauea Volcano, Hawaii. Geol Soc Am Bull 73:1153–1158.

Opheim JA, Gudmundsson A (1989) Formation and geometry of fractures, and related volcanism, of the Krafla fissure swarm, northeast Iceland. Geol Soc Am Bull 101:1608–1622. doi: 10.1130/0016-7606(1989)101<1608:FAGOFA>2.3.CO;2

Oppenheimer C, Francis P (1997) Remote sensing of heat, lava and fumarole emissions from Erta'Ale volcano, Ethiopia. Int J Remote Sens 18:1661–1692.

Oppenheimer C, Kyle PR (2008) Probing the magma plumbing of Erebus volcano, Antarctica, by open-path FTIR spectroscopy of gas emissions. J Volcanol Geotherm Res 177:743–754.

Orr TR, Poland MP, Patrick MR, et al (2015) Kilauea's 5--9 March 2011 Kamoamoa fissure eruption and its relation to 30+ years of activity from Pu'u "O"o. In: R. Carey, M. Poland, V. Cayol, D. Weis (Eds.), Hawaiian Volcanism: From Source to Surface, American Geophysical Union Geophysical Monograph, Vol. 208, Wiley, Hoboken, New Jersey (2015), pp. 393-420

Palma JL, Blake S, Calder ES (2011) Constraints on the rates of degassing and convection in basaltic open-vent volcanoes. Geochemistry, Geophys Geosystems. doi:

10.1029/2011GC003715

Parcheta C, Fagents S, Swanson DA, et al (2015) Hawaiian Fissure Fountains: Quantifying Vent and Shallow Conduit Geometry, Episode1 of the 1969--1974 Mauna Ulu Eruption. In: R. Carey, M. Poland, V. Cayol, D. Weis (Eds.), Hawaiian Volcanism: From Source to Surface, American Geophysical Union Geophysical Monograph, Vol. 208, Wiley, Hoboken, New Jersey (2015), pp. 369-391

Parcheta CE, Houghton BF, Swanson DA (2012) Hawaiian fissure fountains 1: decoding deposits—episode 1 of the 1969–1974 Mauna Ulu eruption. Bull Volcanol 74:1729–1743.

Parcheta CE, Pavlov CA, Wiltsie N, et al (2016) A robotic approach to mapping post-eruptive volcanic fissure conduits. J Volcanol Geotherm Res 320:19–28.

Patrick MR, Anderson KR, Poland MP, et al (2015) Lava lake level as a gauge of magma reservoir pressure and eruptive hazard. Geology 43:831–834.

Pedersen GBM, Höskuldsson A, Dürig T, et al (2017) Lava field evolution and emplacement dynamics of the 2014--2015 basaltic fissure eruption at Holuhraun, Iceland. J Volcanol Geotherm Res 340:155–169. doi: 10.1016/j.jvolgeores.2017.02.027

Philpotts AR, Philpotts DE (2007) Upward and downward flow in a camptonite dike as recorded by deformed vesicles and the anisotropy of magnetic susceptibility (AMS). J Volcanol Geotherm Res 161:81–94. doi: 10.1016/j.jvolgeores.2006.11.006

Reynolds P, Brown RJ, Thordarson T, Llewellin EW (2016) The architecture and shallow conduits of Laki-type pyroclastic cones: insights into a basaltic fissure eruption. Bull Volcanol 78:1–18. doi: 10.1007/s00445-016-1029-0

Richter DH, Eaton JP, Murata KJ, et al (1970) Chronological narrative of the 1959-60 eruption of Kilauea volcano, Hawaii. US Geol. Surv. Prof. Paper 537.

672 Sigurdsson H (2000) Volcanic episodes and rates of volcanism. In: Encyclopedia of
673 Volcanoes. Academic Press San Diego, CA, pp 271–279
674 Stevenson DS, Blake S (1998) Modelling the dynamics and thermodynamics of volcanic
675 degassing. Bull Volcanol 60:307–317.
676 Stothers RB, Wolff JA, Self S, Rampino MR (1986) Basaltic fissure eruptions, plume heights,
677 and atmospheric aerosols. Geophys Res Lett 13:725–728.
678 Stovall WK, Houghton BF, Harris AJL, Swanson DA (2009) Features of lava lake filling and
679 draining and their implications for eruption dynamics. Bull Volcanol 71:767–780.
680 Sumner JM, Blake S, Matela RJ, Wolff JA (2005) Spatter. J Volcanol Geotherm Res 142:49–
681 65.
682 Swanson DA, Duffield WA, Jackson DB, et al (1979) Chronological narrative of the 1969-71
683 Mauna Ulu eruption of Kilauea Volcano, Hawaii. US Geol. Surv. Prof. Paper 1056.
684 Swanson DA, Fabbi BP (1973) Loss of volatiles during fountaining and flowage of basaltic
685 lava at Kilauea volcano, Hawaii. J Res US Geol Surv 1:649–658.
686 Thorarinsson S, Steinthorsson S, Einarsson T, et al (1973) The eruption on Heimaey, Iceland.
687 Nature 241:372–375.
688 Thordarson T, Self S (1993) The Laki (Skaftár Fires) and Grimsvötn eruptions in 1783-1785.
689 Bull Volcanol 55:233–263.
690 Tilling R., Christian R., Duffield WA, et al (1987) The 1972-1974 Mauna Ulu eruption, Kilauea
691 Volcano: An example of quasi steady-state magma transfer. US Geol Surv Prof Pap
692 1350:405–469.
693 Tilling RI (1987) Fluctuations in surface height of active lava lakes during 1972-1974 Mauna
694 Ulu eruption, Kilauea volcano, Hawaii. J Geophys Res Solid Earth 92:13721–13730.
695 Valentine GA, Gregg TKP (2008) Continental basaltic volcanoes- processes and problems. J

696 Volcanol Geotherm Res 177:857–873.
697 Wadsworth FB, Kennedy BM, Branney MJ, et al (2015) Exhumed conduit records magma
698 ascent and drain-back during a Strombolian eruption at Tongariro volcano, New
699 Zealand. Bull Volcanol 77:1–10. doi: 10.1007/s00445-015-0962-7
700 Walker GPL, Self S, Wilson L (1984) Tarawera 1886, New Zealand a basaltic plinian fissure
701 eruption. J Volcanol Geotherm Res 21:61–78.
702 Whitehead JA, Helfrich KR (1991) Instability of flow with temperature-dependent viscosity:
703 A model of magma dynamics. J Geophys Res Solid Earth 96:4145–4155. doi:
704 10.1029/90JB02342
705 Wilson L, Parfitt EA, Head JW (1995) Explosive volcanic eruptions—VIII. The role of magma
706 recycling in controlling the behaviour of Hawaiian-style lava fountains. Geophys J Int
707 121:215–225. doi: 10.1111/j.1365-246X.1995.tb03522.x
708 Witham F, Llewellin EW (2006) Stability of lava lakes. J Volcanol Geotherm Res 158:321–332.
709 Wolfe EW, Neal C., Bamks N., Duggan T. (1988) Puu Oo Eruption of Kilauea Volcano, Hawaii:
710 Espisodes 1 Through 20, January 3, 1983, Through June 8, 1984. US. Geol. Surv. Prof.
711 Pap. 1463
712 Woods AW (1993) A model of the plumes above basaltic fissure eruptions. Geophys Res Lett
713 20:1115–1118.
714 Wright TL, Kinoshita WT, Peck DL (1968) March 1965 eruption of Kilauea volcano and the
715 formation of Makaopuhi lava lake. J Geophys Res 73:3181–3205.
716 Wunderman R (2002) Report on Nyiragongo (DR Congo). Bull Glob Volcanism Netw. doi:
717 dx.doi.org/10.5479/si.GVP.BGVN200204-223030
718 Wylie JJ, Helfrich KR, Dade B, et al (1999) Flow localization in fissure eruptions. Bull Volcanol
719 60:432–440. doi: 10.1007/s004450050243

Wylie JJ, Lister JR (1995) The effects of temperature-dependent viscosity on flow in a cooled channel with application to basaltic fissure eruptions. J Fluid Mech 305:239–261.

Figure Captions

Figure 1: Location map of Mauna Ulu on the Island of Hawai'i. **(a)** The location of the field area is shown in the black box. **(b)** Google Earth™ aerial image of the Mauna Ulu lava field, for reference the centre of the of view is at 19°21'39.43"N, 155°13'5.68"W. **(c)** Interpreted diagram of the image in (b) showing the surface features of the episode 1 Mauna Ulu eruption.

Figure 2: Schematic tree mould showing the measured features, where the uppermost crust is interpreted to be the lava high-stand surface. The distance from the top of the tree mould to the pre-eruption ground surface – i.e. the inundation depth – was measured using a plumb-bob, dropped down the inside of the mould. The position of the lava high-stand surface and post-eruption ground surface were measured using kinematic GPS. Other quantities were determined by difference.

Figure 3: A labelled portion of the fissure system showing how a continuous profile was constructed from discontinuous fissure segments, using the example of the post-eruption ground surface. The post-eruption ground surface base map used is presented in full in Figure 4(c).

Figure 4: Topographic maps, contoured at 1 m intervals, of the **(a)** pre-eruption ground surface topography prior to the 1969 Mauna Ulu eruption, reconstructed from tree mould

744 depths (195 measurements; black dots), **(b)** lava high-stand (269 measurements) and **(c)** the
745 post-eruption ground surface (383 measurements) produced within ArcMap from kGPS
746 measurements. Not all data points appear in every map, because some tree moulds were
747 broken and had no high-stand crust, and because measurements of the post-eruption
748 ground surface were not restricted to locations with tree moulds. The fissure vents exposed
749 at the surface today are marked in red. Elevations are ellipsoid heights (WGS 84) and not
750 geoid corrected.
751
752 **Figure 5:** Map of lava inundation depth during lava high-stand. The map is produced by
753 subtracting the pre-eruption ground surface (Fig. 4a) from the lava high-stand surface (Fig.
754 4b). The fissure vents that can be observed in the field today are marked in red. Segments of
755 the fissure known to be active during the eruption, identified from the Sandia Labs aerial
756 imagery, are traced in white.
757
758 **Figure 6:** Map of lava drainage depth. The map is produced by subtracting the post-eruption
759 ground surface (Fig. 4c) from the lava high-stand surface (Fig. 4b). The fissure vents that can
760 be observed in the field today are marked in red. Segments of the fissure known to be active
761 during the eruption, identified from the Sandia Labs aerial imagery, are traced in white.
762
763 **Figure 7: (a)** Post-eruption ground surface (i.e. present day topographic map) highlighting
764 the three case study areas discussed in this study. **(b)** Detail of the area considered in case
765 study 1 (Box 1 in (a)). The red lines show the fissure exposed at the surface today, the white
766 lines show segments of fissure that were active during the eruption, and the black lines
767 represent the analysed profiles, constructed according to the methodology presented in

768 "Methods: Profile Production" and Figure 3. **(c)** An extract from Figure 5 with arrows
769 showing areas where drainage focused into and around segments of now-buried fissure. **(d)**
770 Profiles for drainage (blue) and inundation depth (orange) across Box 1. Blue vertical dashed
771 lines represent a step from one fissure segment to another, red shaded regions mark fissure
772 segments left exposed at the surface today, and white regions mark areas where the fissure
773 is no longer exposed. **(e)** A field photograph of case study 1 (looking east; direction shown
774 by arrow in part (b)) showing the large western basin depression.
775
776 **Figure 8: (a)** Detail of the area considered in case study 2 (Box 2 in Fig. 7a). The red lines
777 show the fissure exposed at the surface today, the white lines show segments of fissure that
778 were active during the eruption, and the black lines represent the analysed profiles. **(b)**
779 Profiles for drainage (blue) and inundation depth (orange) across Box 2; arrows mark two
780 maxima in the drainage profile. **(c)** Profiles A-A' (dashed) and B-B' (solid) of the pre-eruption
781 ground surface. Vertical red lines mark the intersection between: (i) the A-A' profile (dashed
782 red); (ii) the B-B' profile (solid red) and the fissure.
783
784 **Figure 9:** Fountain height from a linear vent as a function of ponding depth above the vent
785 (data taken from Table 3 of Wilson et al., 1995). The eruption is modelled to have a mass
786 flux of 10^2 kgs^{-1} per meter of fissure with variable exsolved water contents (represented by
787 sequential grey lines). The curves have no physical meaning and are included to guide the
788 eye. For the ponding depths reported in this study (0 to 6 m), it is clear that a dramatic
789 reduction in fountain height would have occurred as ponding depth increased.
790

Figure 10: (a) Detail of the area considered in case study 3 (Box 3 in Fig. 7a). The red lines show the fissure exposed at the surface today, the white lines show segments of fissure that were active during the eruption, and the black lines represent the analysed profiles. **(b)** Lava inundation map of the same area in box 3. The colour scale is the same as for Figure 4, hotter colours representing greater lava inundation depths (5 m maximum, 0 m minimum in inset). **(c)** Elevation profiles of the lava high-stand surface, and pre-eruption and post-eruption ground surface. **(d)** Profiles for drainage (blue) and inundation depth (orange) across Box 3.

Figure 11: A simplified schematic of the interaction between the surface and subsurface processes operating during a fissure eruption. In areas where there was a pre-eruption topographic low (A), the lava is able to inundate and cause deep ponding over the vent. Ponding supresses the subsurface upwelling flux and focuses flow along strike to areas of shallow inundation; these are palaeo- topographic high points (B) and regions with good external drainage/ outflow (C). These localization regions are often preserved as open 'vents' post-eruption.

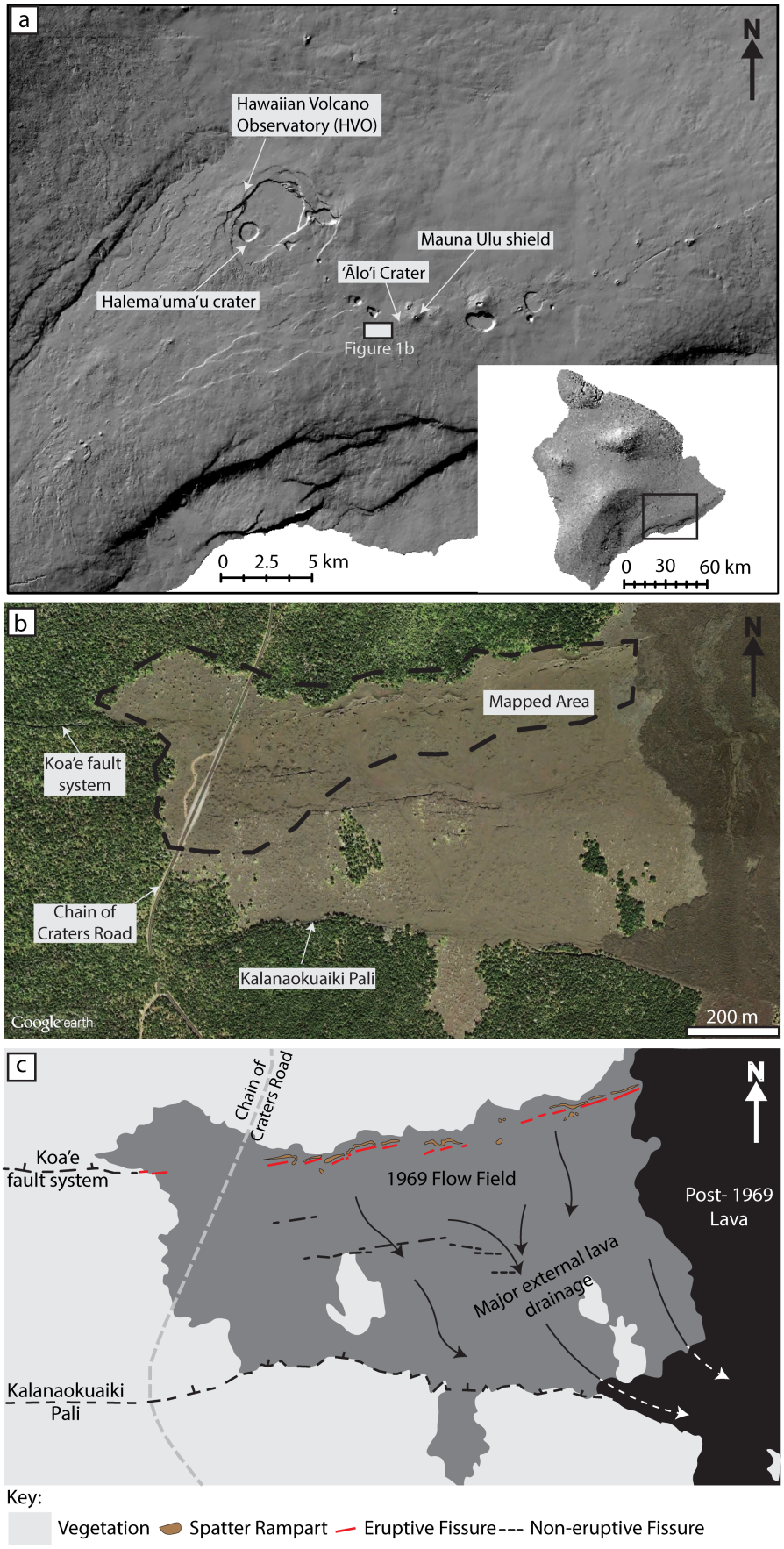
a
N
Hawaiian Volcano Observatory (HVO)
Mauna Ulu shield
'Ālo'i Crater
Halema'uma'u crater
Figure 1b
0 2.5 5 km
0 30 60 km
b
N
Mapped Area
Koa'e fault system
Chain of Craters Road
Kalanaokuaiki Pali
Google earth
200 m
c
N
Chain of Craters Road
Koa'e fault system
1969 Flow Field
Post- 1969 Lava
Major external lava drainage
Kalanaokuaiki Pali
Key:
Vegetation
Spatter Rampart
Eruptive Fissure
Non-eruptive Fissure

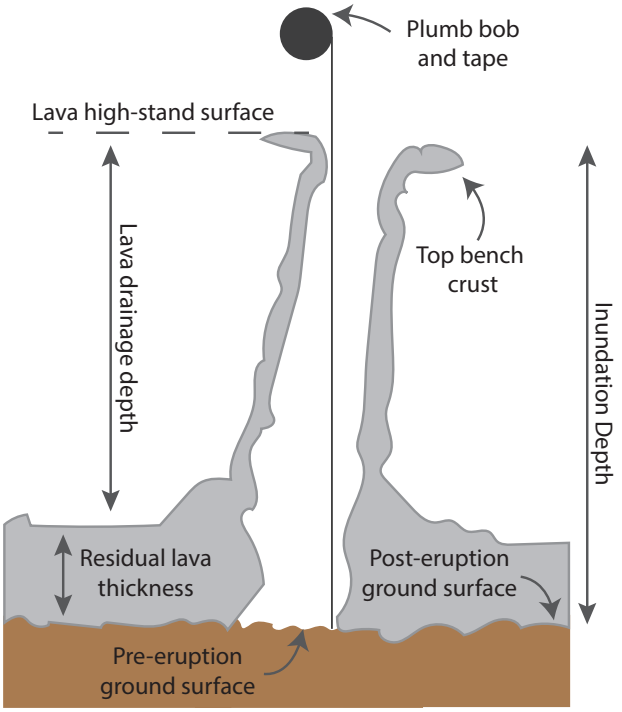

Figure 2: [Jones et al., 2017; Bull Volc.]

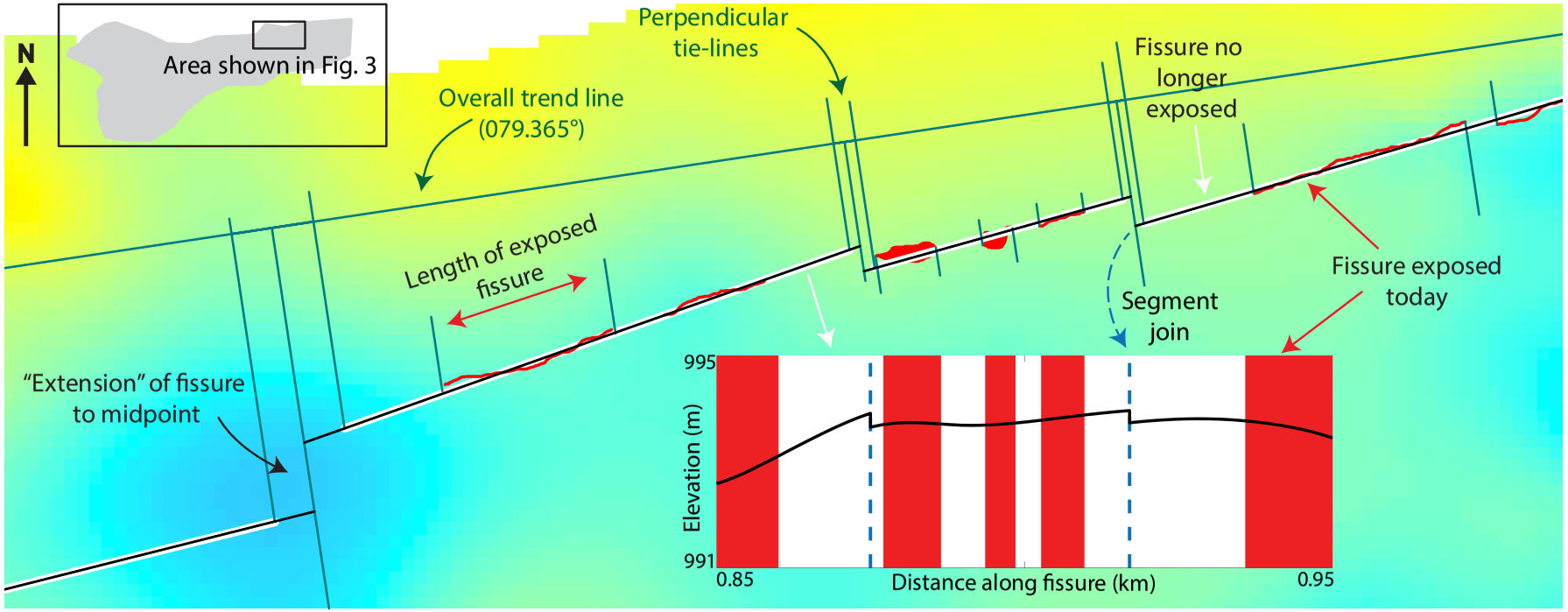

Figure 3: [Jones et al., 2017; Bull. Volc.]

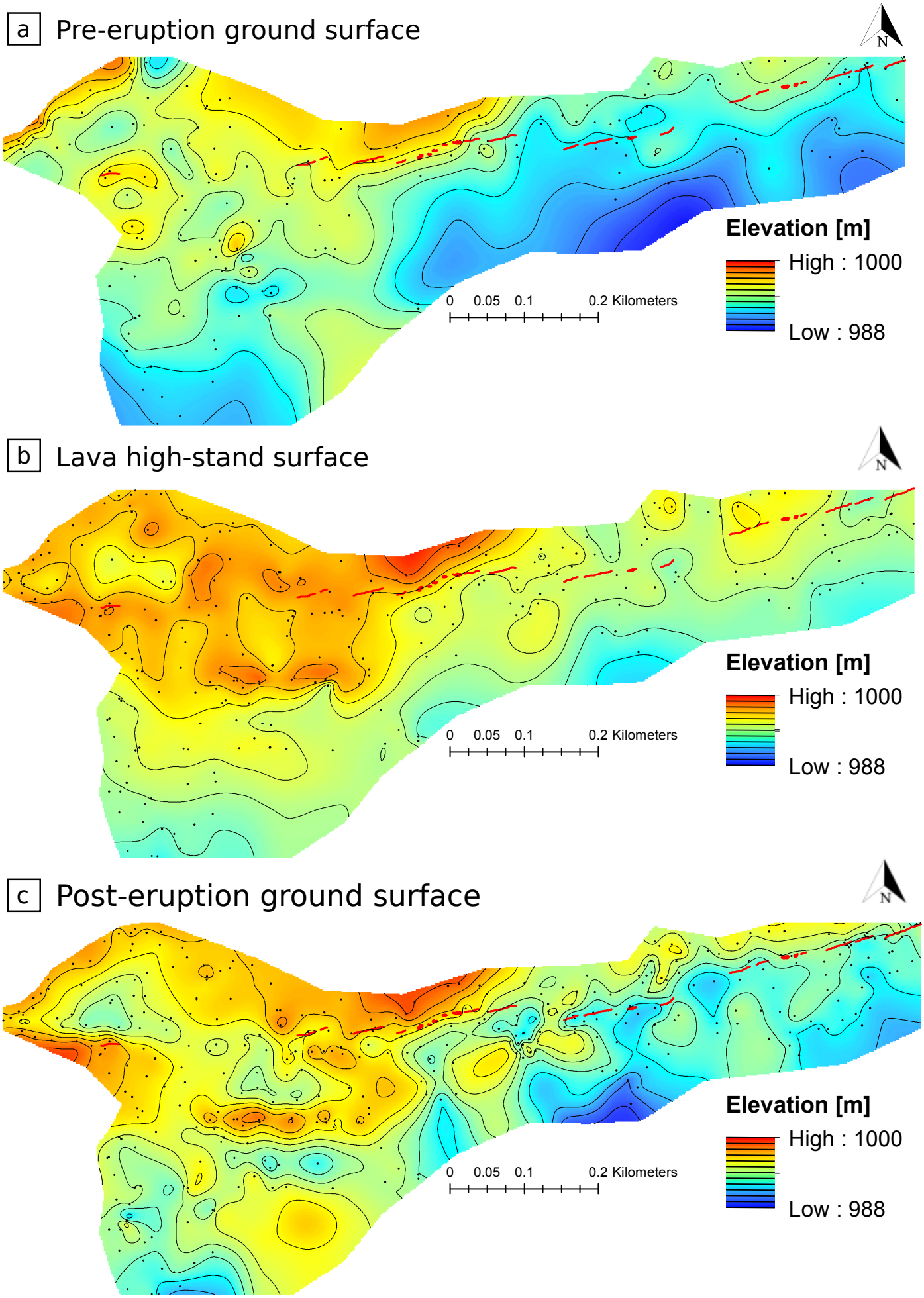

Figure 4: [Jones et al.,2017; Bull Volc]

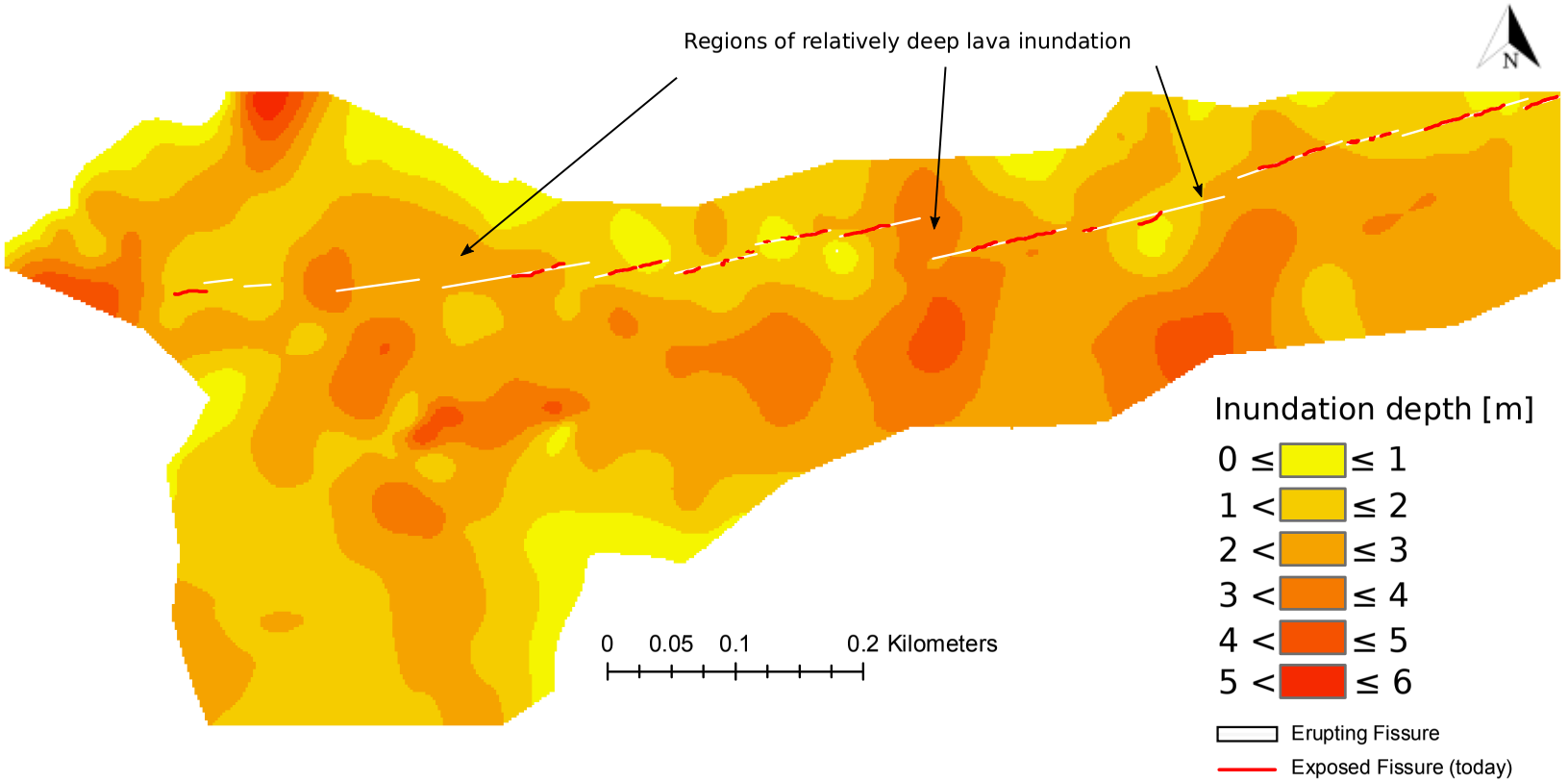

Figure 5: [Jones et al., 2017; Bull Volc.]

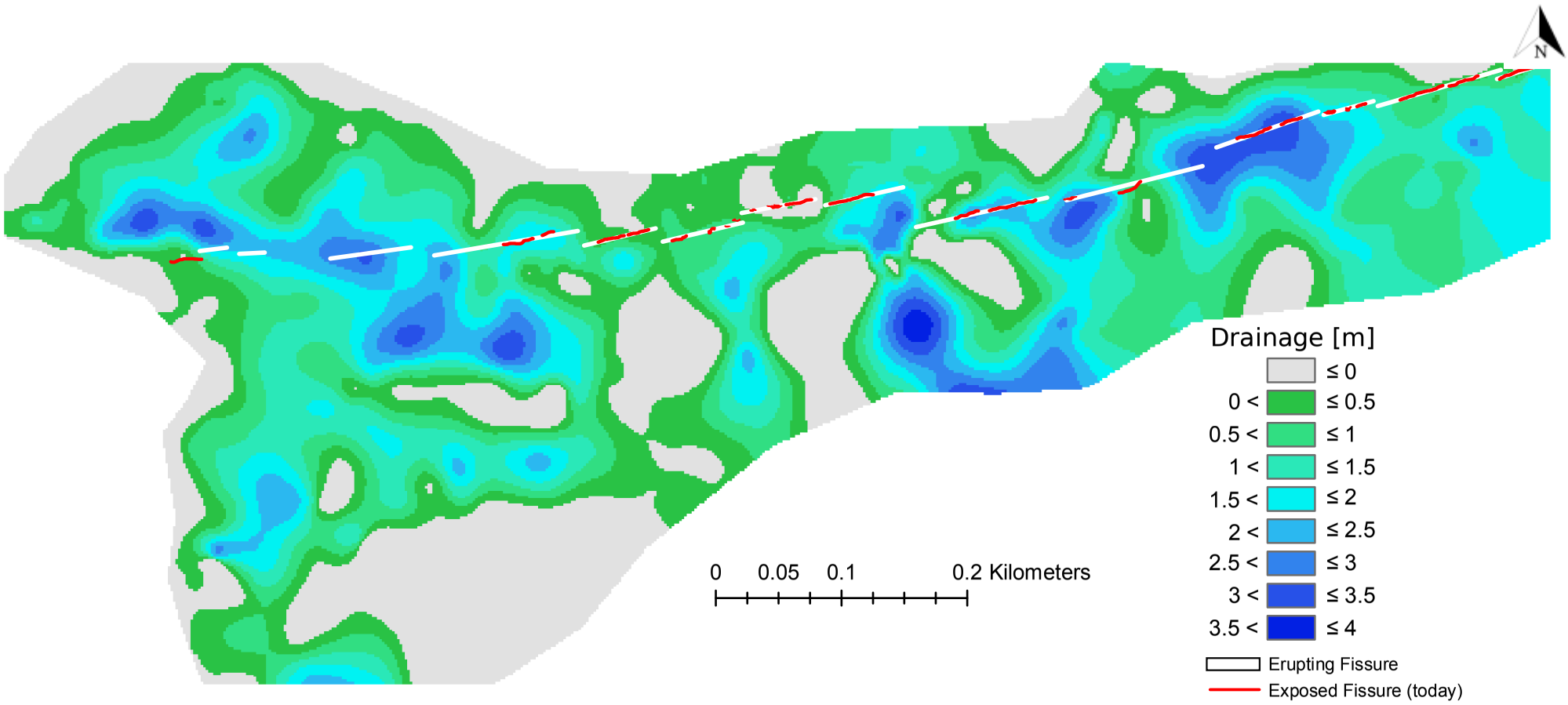

Figure 6: [Jones et al., 2017; Bull Volc.]

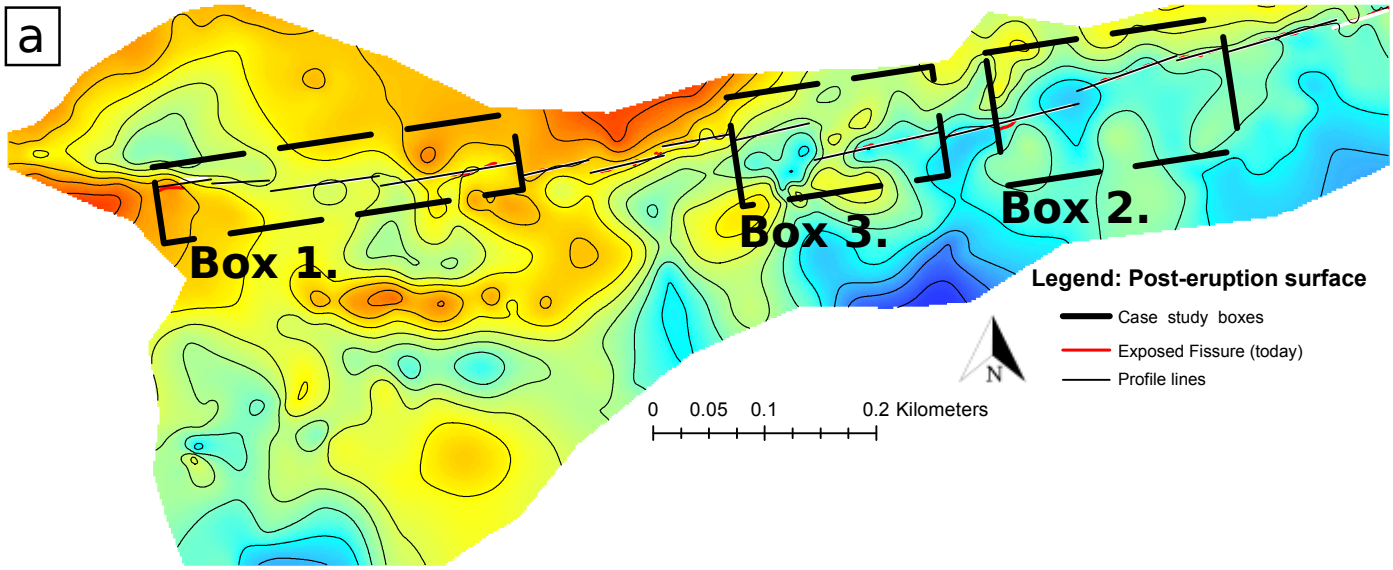

Case study 1:

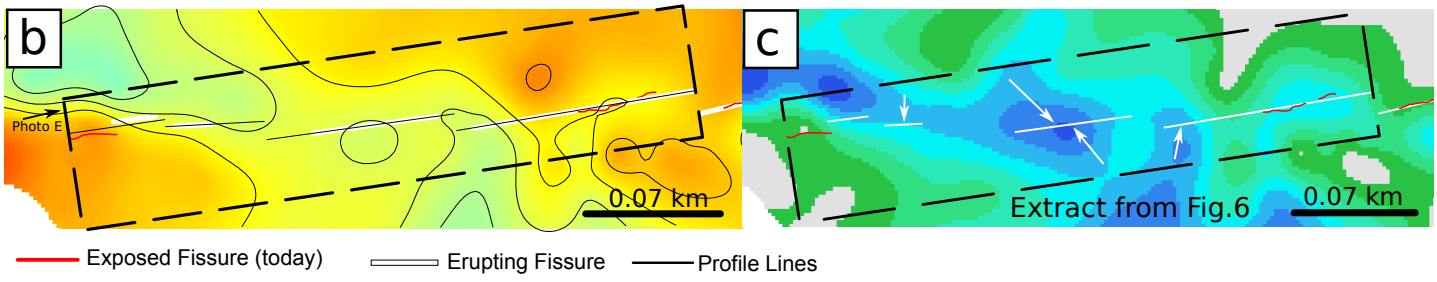

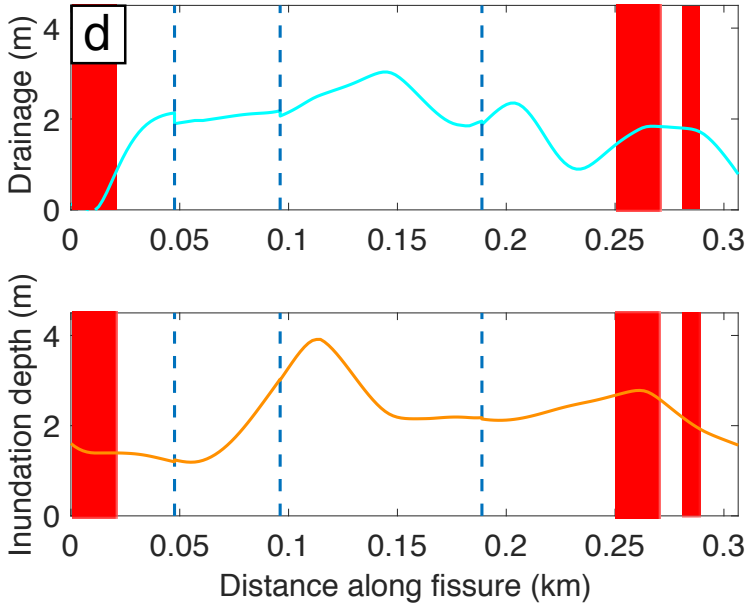

Figure 7: [Jones et al., 2017; Bull Volc.]

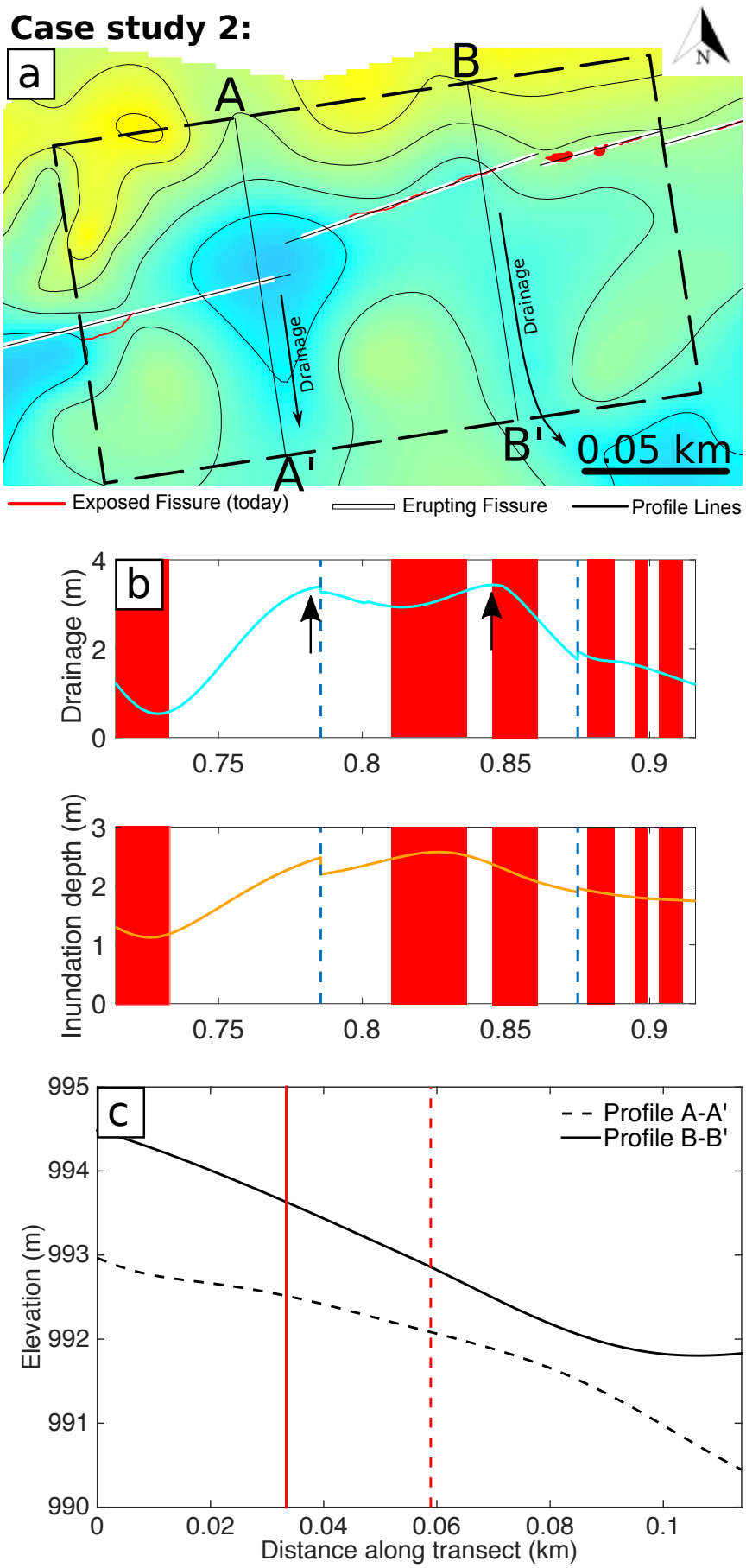

Figure 8: [Jones et al., 2017; Bull Volc.]

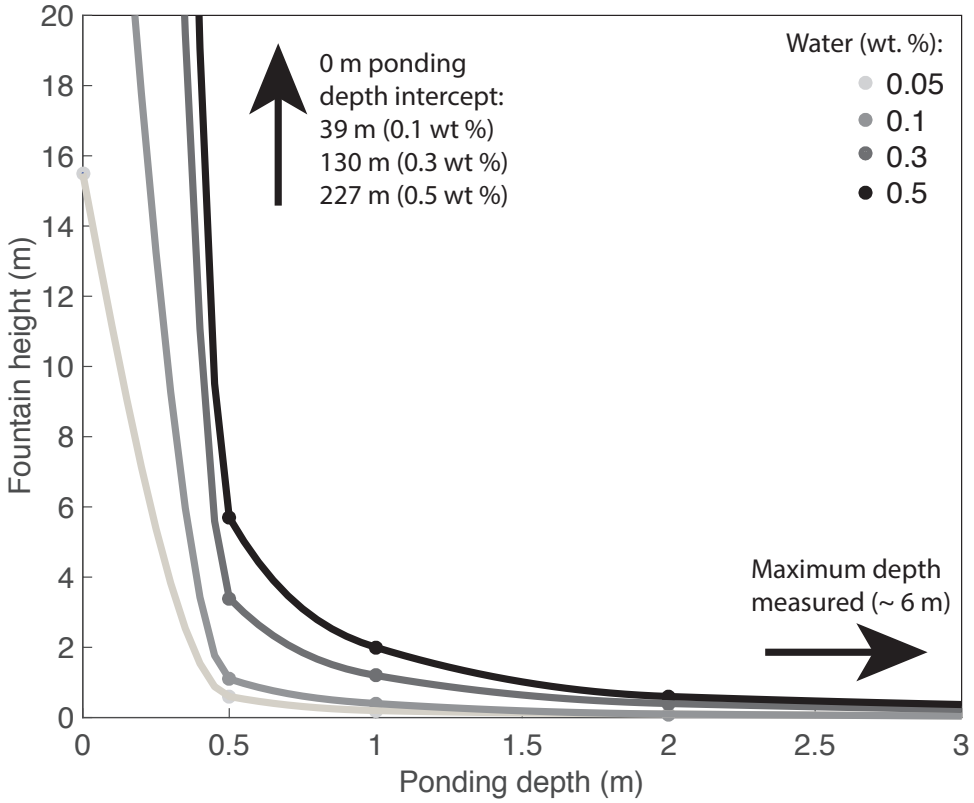

Figure 9: [Jones et al., 2017; Bull. Volc.]

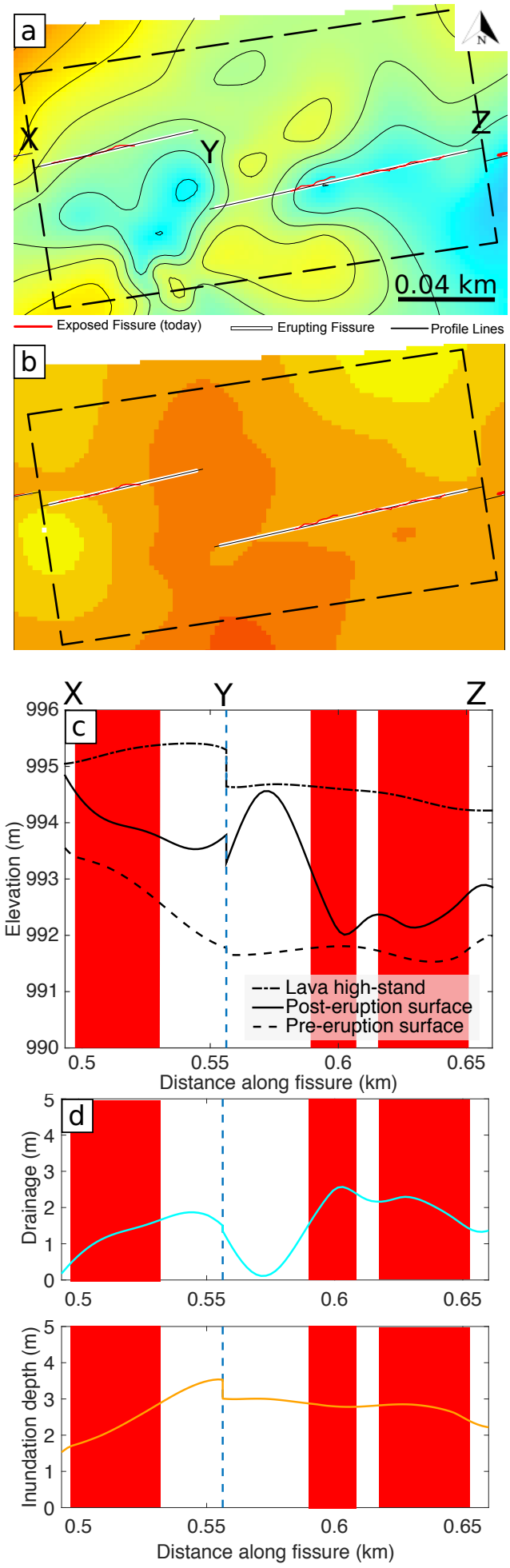

Figure 10: [Jones et al., 2017; Bull Volc.]

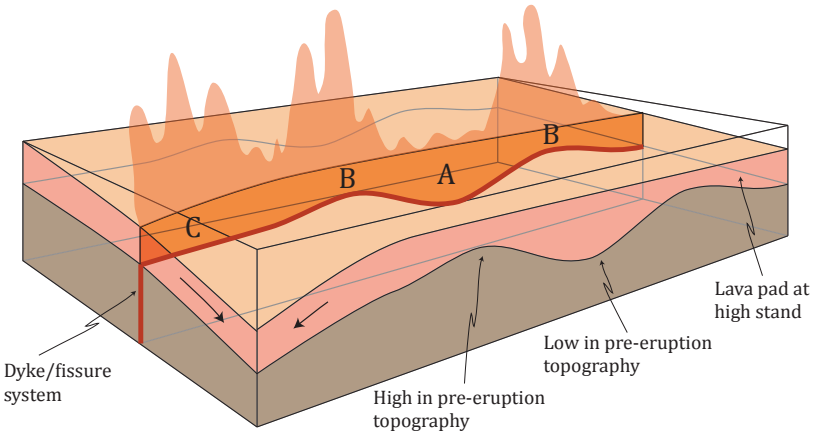

Figure 11: [Jones et al., 2017; Bull Volc.]

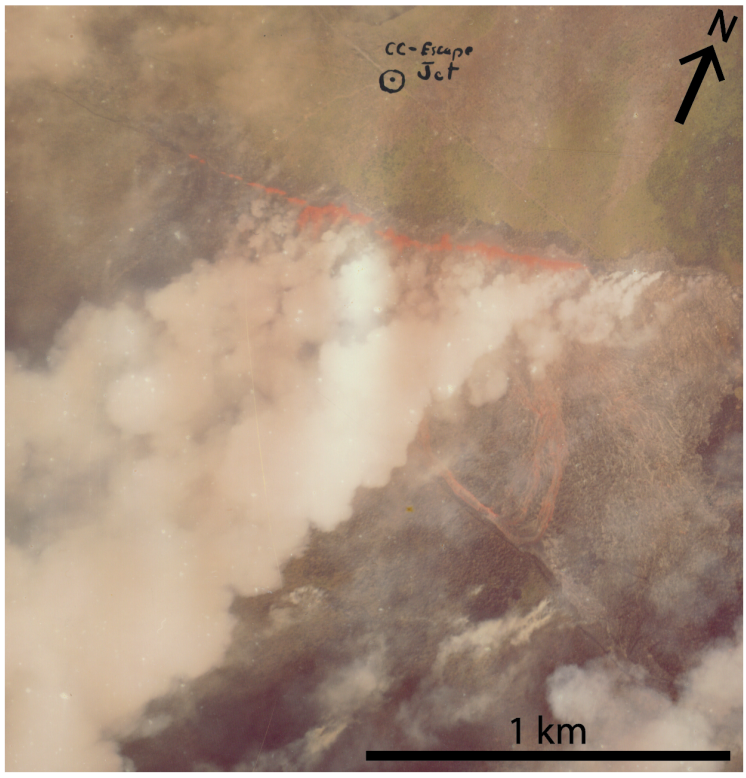

Figure S1: Aerial photograph taken by Sandia Labs at 0940 HST; approximately 1 hour after the fissure reached its full length.

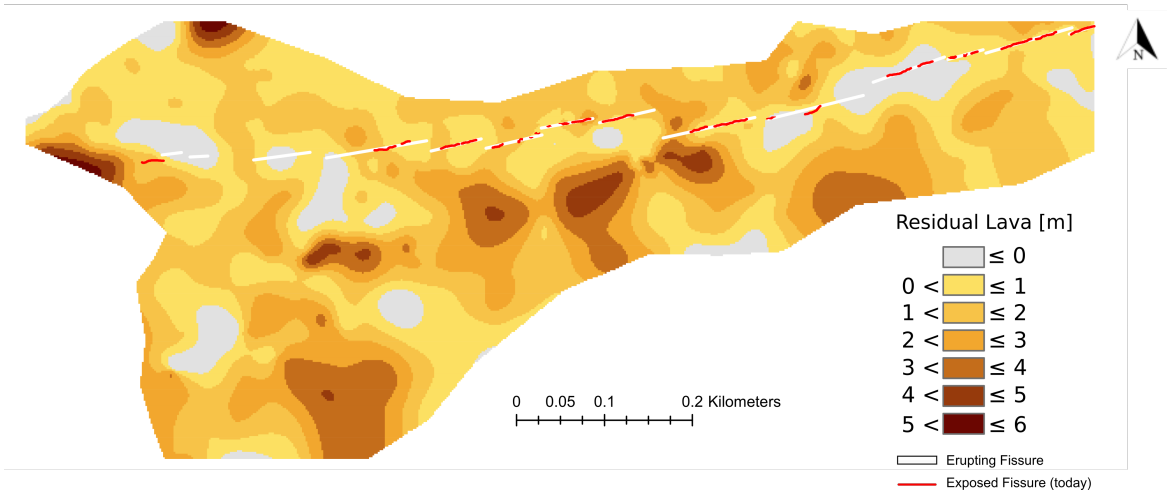

Figure S2: Map of residual lava thickness. The map is produced by subtracting the post-eruption ground surface (Fig. 4c) from the pre-eruption ground surface (Fig. 4a).